

Omnidirectional Images as Moving Camera Videos

Xiangjie Sui, Kede Ma, *Member, IEEE*, Yiru Yao, and Yuming Fang, *Senior Member, IEEE*

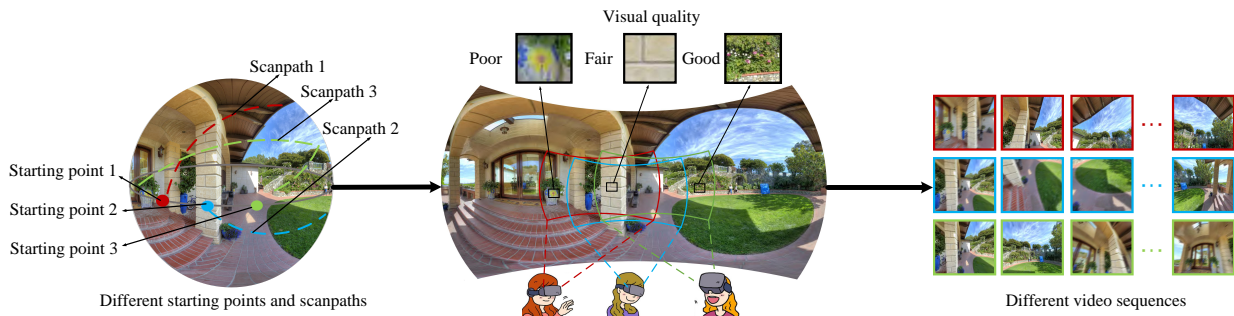


Fig. 1. Illustration of how humans explore static omnidirectional panoramas. Each user may exhibit different viewing behavior, giving rise to different video representations of the same 360° image with varied perceived quality. We considered three types of viewing behavior - starting point, exploration time, and scanpath. Specifically, the starting point provides the longitude and latitude, where the initial viewport can be extracted. A gaze scanpath is generated, when each user is freely exploring the virtual environment within the exploration time. A video sequence, that contains only global motion, can then be obtained by sampling, along each user's scanpath, a number of viewports from the omnidirectional panorama. We computed the perceived quality of the omnidirectional image by comparing to its reference using existing video quality measures.

Abstract—Omnidirectional images (also referred to as static 360° panoramas) impose viewing conditions much different from those of regular 2D images. A natural question arises: how do humans perceive image distortions in immersive virtual reality (VR) environments? We argue that, apart from the distorted panorama itself, three types of viewing behavior governed by VR conditions are crucial in determining its perceived quality: starting point, exploration time, and scanpath. In this paper, we propose a principled computational framework for objective quality assessment of 360° images, which embodies the threefold behavior in a delightful way. Specifically, we first transform an omnidirectional image to several video representations using viewing behavior of different users. We then leverage the recent advances in full-reference 2D image/video quality assessment to compute the perceived quality of the panorama. We construct a set of specific quality measures within the proposed framework, and demonstrate their promises on two VR quality databases.

Index Terms—Omnidirectional images, image quality assessment, virtual reality

1 INTRODUCTION

Virtual reality (VR) photography is the art of capturing or creating a complete natural scene as a single omnidirectional image [1], also known as a static 360° panorama. The viewing experiences enabled by omnidirectional images are substantially different from traditional multimedia data, as humans are allowed to freely explore immersive virtual environments (see Fig. 1). Therefore, understanding how humans perceive visual distortions of omnidirectional panoramas emerges as a new research direction due to its importance to panoramic image acquisition, compression, storage, transmission, and reproduction [2].

Since omnidirectional images are often projected onto 2D rectangular planes for storage (see Fig. 2), it is tempting to adopt existing 2D image quality assessment (IQA) models [3] to quantify perceived distortions in the projections. However, different map projections come with different problems. For example, equirectangular projection generates severe shape distortions near the poles, whereas cube map projection has an oversampling rate of up to 190% compared to the sphere [4]. It follows that distortions measured in the 2D plane may be of weak perceptual relevance to distortions observed in the sphere. To combat

the mismatch between the planar and spherical spaces, several objective IQA models [5, 6] make local quality measurements in the plane, and pool them using spherical areas as weightings to obtain an overall quality score. A better implementation of this similar idea is to compute quality estimates uniformly over the sphere [7, 8].

In 2D IQA, the behavior of users can be well controlled in a laboratory environment, and is often assumed to be similar without explicit modeling. However, this assumption does not hold in omnidirectional IQA. Equipped with a head-mounted display (HMD), humans are able to use both significant head and gaze movements to explore viewports of interest in the scene. Recently, Sitzmann *et al.* [9] found that agreement among gaze scanpaths of subjects exploring 22 panoramas is not consistently high. To the best of our knowledge, no existing IQA model gives a complete treatment of viewing behavior when predicting the perceived quality of omnidirectional images.

To develop a reliable objective IQA model for omnidirectional images, it is crucial to model visual exploration behavior during the quality assessment process. In this work, we take steps towards this goal in the full-reference IQA setting [3]. We argue that there are at least three types of viewing behavior that play an important role in omnidirectional IQA: starting point, exploration time, and scanpath. The starting point provides the longitude and latitude, at which the initial viewport is centered (see Fig. 2); the exploration time records how long it takes for a user to finish exploring an omnidirectional image; the scanpath is a 2D trajectory of the eyes over the sphere when scanning the visual field [10]. For different viewers, we propose to represent an omnidirectional image by different moving camera videos, where we sample, along each user's scanpath, a sequence of rectilinear projections of viewports. The resulting video sequences contain only global

- Xiangjie Sui, Yiru Yao, and Yuming Fang are with the School of Information Technology, Jiangxi University of Finance and Economics, Nanchang 330032, Jiangxi, China (e-mail: suixiangjie2017@163.com, 2848444870@qq.com, fa0001ng@e.ntu.edu.sg).
- Kede Ma is with the Department of Computer Science, City University of Hong Kong, Kowloon, Hong Kong 999077, China (e-mail: kede.ma@cityu.edu.hk).

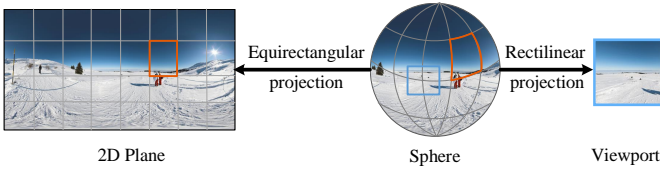


Fig. 2. Illustration of different representations of an omnidirectional image. Equirectangular projection is commonly used to obtain a 2D plane for storage, while rectilinear projection is adopted to extract a viewport for visual consumption at a time instant.

motion [11], as if they were captured by a moving camera, where the moving patterns are determined by users’ viewing behavior. When such information is not available, the video representations of a 360° image may be obtained by assuming a set of preferable user behavior.

Instead of learning omnidirectional IQA models from scratch, the novel video representations of 360° images allow us to directly adopt existing video quality assessment (VQA) tools to this immersive application. Here we construct several computational models within the proposed quality assessment framework by first predicting frame-level quality using existing 2D IQA models [3], and then pooling the quality estimates [12] by considering cognitive effects of the human brain [13]. Our extensive experiments based on two publicly available VR databases [14, 15] lead to two main findings. First, surprisingly, advanced 2D IQA models [16–18] that work directly with equirectangular projections (at a proper scale), outperform those [5, 7, 8, 19] tailored to omnidirectional IQA by a clear margin. Second, the proposed quality assessment framework achieves significant performance improvements for a wide range of 2D IQA models [16–18, 20], when applying them to video representations (rather than equirectangular projections) of 360° panoramas.

2 RELATED WORK

In this section, we first introduce subjective user studies of omnidirectional images. We then briefly describe 2D IQA/VQA methods that serve as building blocks of the proposed framework. Last, we review IQA models that are specifically designed for omnidirectional images.

2.1 Subjective Quality Assessment of Panoramic Images

Since the human eye is the ultimate receiver of omnidirectional images, the most trustworthy way of evaluating their visual quality is through subjective testing. Upenik *et al.* [21] constructed one of the first VR IQA databases to study the impact of compression and projection on the visual quality of panoramas. The absolute category rating was adopted to collect the mean opinion score (MOS) of each image, where a higher MOS means better perceived quality. Additionally, head movement (HM) data were also recorded for visual saliency map computation. Duan *et al.* [14] built a high-resolution VR IQA database with four distortion types. Apart from the HM data, eye movement (EM) data were recorded for human behavior analysis in such immersive environments. They reported that the majority of 2D IQA methods are insufficient to provide accurate quality predictions. Sun *et al.* [22] proposed so far the largest VR IQA database, consisting of 528 impaired omnidirectional images produced from 16 references. Huang *et al.* [23] studied the joint effect of spatial resolution and JPEG compression on the perceived quality of 360° images. Recently, Chen *et al.* [15] conducted subjective quality assessment of stereoscopic omnidirectional panoramas. The detailed information of these databases is summarized in Table 1.

Although several databases included user behavior statistics (*i.e.*, HM/EM data), no timestamp information was found. As a consequence, it is difficult to recover user viewing behavior (*e.g.*, starting point and scanpath), which, we consider, are indispensable in omnidirectional IQA. Besides, existing subjective experiments were carried out on visual materials with global uniform distortions. Little investigation is dedicated to local non-uniform distortions, which may have a different impact on how subjects explore and perceive the virtual scenes.

2.2 Full-Reference Quality Assessment of 2D Images and Videos

Full-reference IQA and VQA involve developing computational models that are capable of automatically predicting the perceptual quality of images and videos, by comparing to their pristine references. Most full-reference IQA/VQA models are designed for 2D image and videos, among which the mean squared error (MSE), or its derivative peak signal-to-noise ratio (PSNR), is the most widely used. MSE calculates the absolute differences of pixels between the original and distorted images, and is shown to be poorly correlated with human perception of image quality. Later methods tried to model aspects of the human visual system (HSV) or treated it as a “black box” with some holistic assumptions, with the structural similarity (SSIM) index [20] being the most successful. Recently, there has been a surge of interest in leveraging hierarchical representations of deep neural networks (DNNs) for the design of IQA metrics. Johnson *et al.* [24] used the MSE computed on convolution responses of pre-trained DNNs to guide the optimization of image super-resolution algorithms. Zhang *et al.* [25] demonstrated the perceptual relevance of deep features pre-trained from a wide range of vision tasks. Ding *et al.* [18] developed an IQA metric with explicit tolerance to visually similar textures.

Compared with IQA, objective quality assessment of video sequences is more challenging due to complex interactions between spatial and temporal distortions. A simple and computationally efficient solution is to compute frame-level quality scores by IQA methods, followed by temporal pooling. Tu *et al.* [12] conducted an empirical comparison of the effectiveness of different temporal pooling strategies. Another type of VQA methods attempted to directly extract spatiotemporal features for quality prediction. Zeng *et al.* [26] proposed a spatiotemporal SSIM index by treating video signals as 3D volume data. Kim *et al.* [27] developed a DNN-based full-reference VQA method by incorporating spatiotemporal human visual perception. Xu *et al.* [28] presented a spatiotemporal feature learning framework, where a DNN with 3D convolution kernels was used to learn spatiotemporal distortion thresholds.

2.3 Objective Quality Assessment of Panoramic Images

Nearly all quality measures for panoramas adapted existing 2D IQA methods to three formats - 2D plane, sphere, and viewport. Methods [5, 6] in the 2D plane tried to compensate the non-uniform sampling due to sphere-to-plane projection. Take equirectangular projection as an example. The local quality measure is weighted by $\cos(\theta)$, where θ is the corresponding latitude of the local pixel/patch in spherical domain. In [19], Craster parabolic projection was employed to guarantee uniform sampling density. However, map projections are likely to cause geometric deformations (see Fig. 2). The second type of methods such as S-PSNR [7] and S-SSIM [8] computed local quality estimates uniformly in the sphere. Yu *et al.* [7] proposed two variants of S-PSNR by deriving importance weightings from statistical distributions of the HM/EM data. The third type of methods [29, 30] focused on extracting viewports that are highly likely to be explored by viewers by exploiting the HM/EM data.

The above methods [5–8, 19, 29, 30] are meaningful attempts to omnidirectional IQA. However, most build their models on top of traditional 2D IQA models such as PSNR and SSIM, ignoring years of model improvement in this field, where more robust and accurate models are available. Moreover, they fail to take user viewing behavior into account, making quality assessment ineffective.

3 PROPOSED FRAMEWORK

In this section, we describe a general computational framework for omnidirectional IQA, where user viewing behavior is incorporated naturally by considering omnidirectional images as moving camera videos, as shown in Fig. 3.

3.1 Input Data

The input data to our computational model consist of 1) a pair of (possibly projected) reference and distorted panoramas and 2) three viewing behavior statistics, including:

| Database | Projection | # of images | Resolution | Exploration time | HM/EM data | Distortion type | Public availability |
|---------------------------|------------|-------------|--------------------------------------|------------------|------------|---|---|
| Upenik <i>et al.</i> [21] | ERP CMP | 6/54 | 3,000×1,500 (ERP) 2250×1500 (CMP) | 30 | HM | JPEG compression, Projection | N/A |
| Duan <i>et al.</i> [14] | ERP | 16/320 | 11,332×5,666 to 13320×6660 | 20 | HM and EM | JPEG compression, JPEG2000 compression, Gaussian blur, Gaussian noise | Upon request |
| Sun <i>et al.</i> [22] | ERP | 16/528 | 4,096×2,048 | N/A | N/A | JPEG compression, H.264 compression, H.265 compression | N/A |
| Huang <i>et al.</i> [23] | ERP | 12/144 | 4,096×2,160 | 20 | N/A | Downsampling, JPEG compression | https://vision.nju.edu.cn/20/87/c29466a467079/page.html |
| Chen <i>et al.</i> [15] | ERP | 15/450 | 4,096×2,048 | 20 | HM and EM | Gaussian noise, Gaussian blur, Downsampling, Stitching distortion, VP9 compression, H.265 compression | http://live.ece.utexas.edu/research/VR3D/index.html |

Table 1. Summary of subjective VR IQA databases. ERP and CMP stand for the equirectangular projection and the cube map projection, respectively. The data in the “# of images” column are in the format of “# of reference images/# of distorted images”.

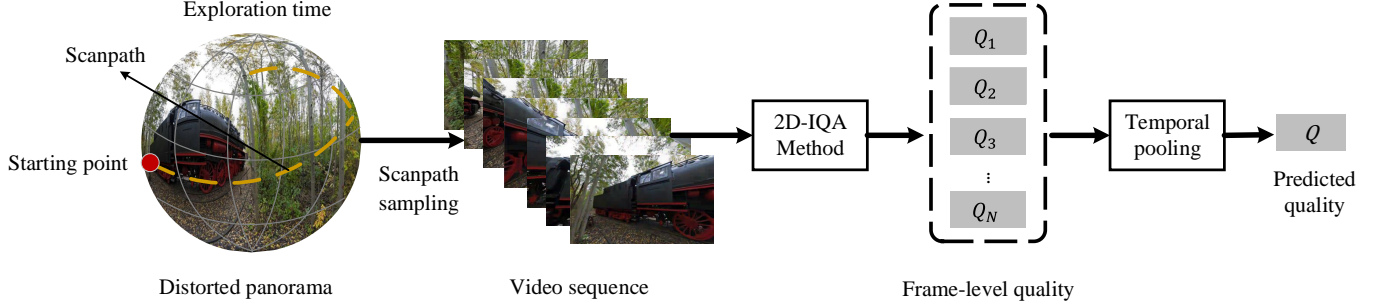


Fig. 3. Proposed computational framework for omnidirectional IQA. The processing of the reference panorama has been omitted for simplicity.

- **The starting point**, $P_0 = (\phi_0, \theta_0)$, specifies the longitude and latitude, at which the initial viewport is centered for a viewer to start exploring the virtual scene. Sitzmann *et al.* [9] showed that different starting points may have different impacts on visual saliency in VR, therefore affecting how humans perceive the quality of the same scene. Moreover, with varied starting points, the scanpath and exploration time may be different among users due to differences in personalized viewing experience. Some examples of different starting points are shown in Fig. 4.
- **The exploration time**, T , records how long it takes for a viewer to explore the panorama. Assuming a reasonable gaze speed, a short exploration time means that the user may only observe a few viewports, highlighting the importance of the starting point in the quality assessment process. By contrast, with a long exploration time, the viewer is more likely to be influenced by viewports close to the end of viewing due to the recency effect [31].
- **The scanpath** $P(t) : \mathbb{R} \mapsto \mathbb{R}^2$, describes a 2D trajectory of the user’s eyes when exploring the visual field [10]. It takes a time instant $t \in [0, T]$ as input, and produces a 2D spherical coordinate (ϕ, θ) , where $P(0) = (0, 0)$. The viewport at a specific time instant t can be extracted at $P(t) + P_0$.

3.2 Omnidirectional Images to Videos Conversion

Given the viewing behavior of a user, we are able to convert a panorama into a video sequence, which contains only global motion as if the underlying static scene was captured by a moving camera. This is achieved by sampling a sequence of rectilinear projections of viewports of the panorama along the scanpath [32], with a predefined sampling rate. Specifically, given the current sample point $P(t) + P_0$ as the center, we first set the field of view (FoV) to $[-\pi/6, \pi/6]$ along both longitude and latitude directions, inspired by the theory of near peripheral vision [33]. This specifies 3D Cartesian coordinates of the square viewport, which is assumed to be perpendicular to the Z-axis for convenience. The corresponding pixel values can be retrieved by projecting 3D Cartesian

points onto points on the unit sphere and then points on the projected 2D plane. Bicubic interpolation is used as the optional resampling filter. We then choose a sampling rate

$$R = \frac{1}{s_1} \times R_{et}, \quad (1)$$

where R_{et} is the maximum sampling rate constrained by the eye tracker and $s_1 \geq 1$ is a stride parameter. The resulting moving camera video has a total of $N = R \times T$ frames.

3.3 Panoramic Picture Quality Prediction

Generally, any existing VQA model could be adopted at this stage to evaluate the perceived quality of 360° images. Here we follow a two-stage approach: frame-level quality estimation followed by temporal pooling. For the i -th viewer, we denote the j -th frames of the corresponding reference and distorted videos by X_{ij} and Y_{ij} , respectively. The frame-level quality can be computed by

$$Q_{ij} = D(X_{ij}, Y_{ij}), \quad (2)$$

where D denotes a full-reference IQA model. The global quality Q_i as perceived by the i -th user can be computed by fusing frame-level quality scores:

$$Q_i = F(Q_{i1}, \dots, Q_{iN}), \quad (3)$$

where F is a temporal pooling strategy that models aspects of the memory effect of humans. Similar as computing MOSs, we average quality estimates across all subjects to obtain the final quality score of the panorama:

$$Q = \frac{1}{M} \sum_{i=1}^M Q_i, \quad (4)$$

where M indicates the number of viewers.

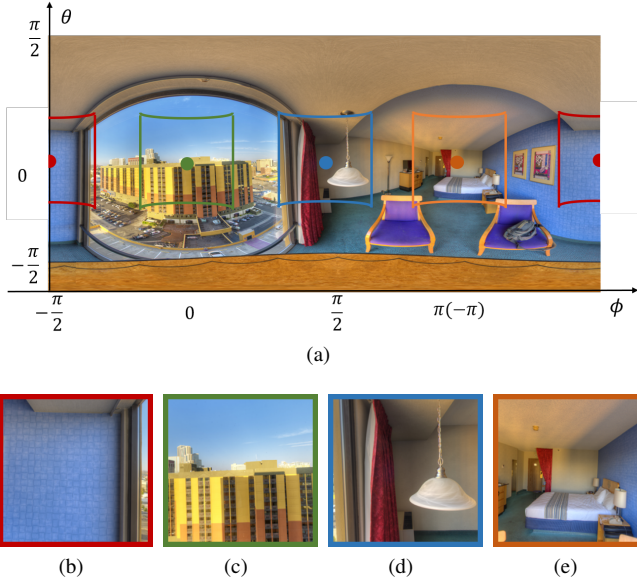


Fig. 4. Examples of viewports extracted from different starting points. (a) Original panorama in equirectangular projection format. (b)-(e) Viewports corresponding to the starting points $(-\frac{\pi}{2}, 0)$, $(0, 0)$, $(\frac{\pi}{2}, 0)$, and $(\pi, 0)$, respectively.

3.4 Specific Omnidirectional IQA Models

We constructed several specific examples of omnidirectional IQA measures within the proposed framework. First, we needed to specify 2D IQA models for computing frame-level quality. The main selection criterion is that the model should correlate well with human perception of image quality, in terms of *benchmarking* as well as *optimizing* image processing algorithms. In this paper, we selected five full-reference image quality models:

- PSNR, the Peak Signal-to-Noise Ratio, is built on top of the MSE by incorporating the maximum power of a signal. Arguably the PSNR (or MSE) is the most widely used IQA measure, and enjoys a number of desirable properties for optimization purposes.
- SSIM [20], the Structural SIMilarity index, assumes the HVS is highly adapted to extract local image structures of the visual field. Thus, a measure of structural information loss may provide a good approximation to perceived quality degradation. Over the years, SSIM and its multi-scale extension [34] have been regarded as standard “perceptual” metrics to guide the optimization of computational methods for image denoising [35], image compression [36], image synthesis [37], and video coding [38].
- VIF [16], the Visual Information Fidelity measure, offers an information theoretical perspective of IQA, and uses the mutual information [39] to quantify the amount of information preserved in the distorted image. VIF is capable of producing an image of enhanced local contrast than the original. Its industrial implementation - VMAF [40] has been successfully applied to adjust the parameter settings in video engineering.
- NLPD [17], the Normalized Laplacian Pyramid Distance, is based on a multi-scale nonlinear representation that models the operations in early stages of the HVS (*i.e.*, the retina and lateral geniculate nucleus). NLPD has been used to optimize tone mapping algorithms, where the input image has a much higher dynamic range (in the unit of candela per square meter) than that of the output image [17].
- DISTS [18], the Deep Image Structure and Texture Similarity metric, uses a DNN to construct an injective and perceptual transform, and makes SSIM-motivated quality measurements in the

| Viewing behavior | Value |
|------------------|---|
| P_0 | $\{(-\frac{\pi}{2}, 0), (0, 0), (\frac{\pi}{2}, 0), (\pi, 0)\}$ |
| T | 15 seconds |
| $P(t)$ | $\phi = \begin{cases} -vt, 0 \leq t \leq \frac{T}{4} \\ -\frac{\pi}{2} + v(t - \frac{T}{4}), \frac{T}{4} < t \leq \frac{3T}{4}, & \theta = 0 \\ \frac{\pi}{2} - v(t - \frac{3T}{4}), \frac{3T}{4} < t \leq T \end{cases}$ |

Table 2. Default user viewing behavior for panoramic image-to-video conversion. (ϕ, θ) are the longitude and latitude, and v is gaze velocity defined in Eq. (11).

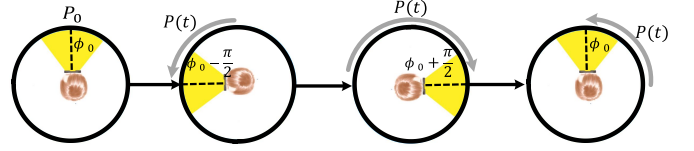


Fig. 5. Illustration of the default scanpath. ϕ_0 is the longitude of the starting point.

transform domain. DISTS is robust to texture resampling and mild geometric transformations. In a recent comparison of IQA models for optimization of image processing systems [41], DISTS outperforms the ten competing models in blind image deblurring, single image super-resolution, and lossy image compression.

We then adopted the temporal hysteresis model [42] as the default pooling strategy. Specifically, to mimic users’ intolerance to poor quality events and reluctant reaction to quality improvement events, a memory component is defined at each video frame:

$$Q_j^m = \begin{cases} Q_1 & j = 1 \\ \min \{Q_{\max\{1, j-K\}}^m, \dots, Q_{j-2}^m, Q_{j-1}^m\} & \text{otherwise} \end{cases} \quad (5)$$

where we omitted the user index i in the subscript to make the notation uncluttered. K is a parameter related to the duration of memory [42].

The temporal hysteresis pooling also accounts for the fact that humans react sharply to quality degradation events by defining a current quality component at each video frame:

$$Q_j^c = \sum_{k=j}^{\min\{j+K, N\}} w_k Q_k^s, \quad (6)$$

and

$$\{Q_k^s\} = \text{sort} \left(\{Q_k\}_{k=j}^{\min\{j+K, N\}} \right), \quad (7)$$

where $\text{sort}()$ sorts $\{Q_j, \dots, Q_{\min\{j+K, N\}}\}$ in ascending order, resulting in $\{Q_j^s, \dots, Q_{\min\{j+K, N\}}^s\}$. w is a normalized weighting vector specified by the descending half of a Gaussian function. The adjusted time-varying quality score of Y_j is computed by linearly combining the memory and current elements:

$$Q_j^a = \alpha Q_j^m + (1 - \alpha) Q_j^c, \quad (8)$$

where α is a parameter to trade off the two terms. The global quality is obtained by averaging the quality scores of all frames:

$$Q = \frac{1}{N} \sum_{j=1}^N Q_j^a. \quad (9)$$

The proposed framework requires user viewing behavior to transform static panoramas to moving camera videos. When such information is not available, the overall quality score may be obtained by taking the

| | JPEG | | | JP2K | | | GB | | | GN | | | Overall | | |
|---------------|---------------|---------------|---------------|---------------|---------------|---------------|---------------|---------------|---------------|---------------|---------------|---------------|---------------|---------------|---------------|
| | PLCC | SRCC | RMSE |
| S-PSNR | 0.8849 | 0.8468 | 1.0698 | 0.8855 | 0.8865 | 1.0268 | 0.7629 | 0.7796 | 1.2759 | 0.9119 | 0.8813 | 0.7724 | 0.7466 | 0.7507 | 1.4071 |
| S-SSIM | 0.9215 | 0.9033 | 0.8919 | 0.9302 | 0.9314 | 0.8109 | 0.8691 | 0.8696 | 0.9656 | 0.9607 | 0.9414 | 0.5225 | 0.8327 | 0.8225 | 1.1707 |
| WS-PSNR | 0.8925 | 0.8467 | 1.0362 | 0.8844 | 0.8859 | 1.0316 | 0.7831 | 0.7806 | 1.2141 | 0.9117 | 0.8813 | 0.7730 | 0.7466 | 0.7505 | 1.4066 |
| CPP-PSNR | 0.8935 | 0.8493 | 1.0314 | 0.8830 | 0.8846 | 1.0372 | 0.7640 | 0.7644 | 1.2597 | 0.9100 | 0.8782 | 0.7800 | 0.7415 | 0.7468 | 1.4186 |
| PSNR | 0.8938 | 0.8476 | 1.0304 | 0.8901 | 0.8926 | 1.0073 | 0.7562 | 0.7544 | 1.2776 | 0.9224 | 0.8954 | 0.7267 | 0.7270 | 0.7330 | 1.4518 |
| O-PSNR | 0.9022 | 0.8911 | 0.9910 | 0.8999 | 0.9005 | 0.9637 | 0.8878 | 0.8856 | 0.8986 | 0.9133 | 0.8812 | 0.7661 | 0.7681 | 0.7799 | 1.3537 |
| Increase | +0.0084 | +0.0435 | -0.0394 | +0.0098 | +0.0079 | +0.0436 | +0.1316 | +0.1312 | -0.3790 | -0.0091 | -0.0142 | +0.0395 | +0.0407 | +0.0469 | -0.0969 |
| SSIM | 0.9102 | 0.8928 | 0.9515 | 0.9243 | 0.9258 | 0.8436 | 0.8497 | 0.8445 | 1.0293 | 0.9568 | 0.9372 | 0.5471 | 0.8139 | 0.8022 | 1.2285 |
| O-SSIM | 0.9376 | 0.9215 | 0.7987 | 0.9411 | 0.9392 | 0.7474 | 0.9241 | 0.9211 | 0.7463 | 0.9445 | 0.9301 | 0.6179 | 0.8717 | 0.8616 | 1.0361 |
| Increase | +0.0274 | +0.0287 | -0.1527 | +0.0168 | +0.0134 | -0.0962 | +0.0743 | +0.0766 | -0.2830 | -0.0123 | -0.0071 | +0.0708 | +0.0578 | +0.0594 | -0.1924 |
| VIF | 0.9165 | 0.9002 | 0.9187 | 0.9546 | 0.9563 | 0.6583 | 0.9622 | 0.9579 | 0.5319 | 0.9501 | 0.9209 | 0.5871 | 0.8783 | 0.8618 | 1.0109 |
| O-VIF | 0.9377 | 0.9228 | 0.7981 | 0.9690 | 0.9684 | 0.5457 | 0.9675 | 0.9645 | 0.4934 | 0.9533 | 0.9165 | 0.5684 | 0.8957 | 0.8798 | 0.9402 |
| Increase | +0.0212 | +0.0226 | -0.1206 | +0.0144 | +0.0122 | -0.1126 | +0.0054 | +0.0066 | -0.0385 | +0.0032 | -0.0044 | -0.0187 | +0.0174 | +0.0181 | -0.0706 |
| NLPD | 0.9539 | 0.9454 | 0.6895 | 0.9457 | 0.9472 | 0.7182 | 0.8905 | 0.8933 | 0.8881 | 0.9644 | 0.9467 | 0.4976 | 0.8543 | 0.8438 | 1.0989 |
| O-NLPD | 0.9726 | 0.9580 | 0.5342 | 0.9643 | 0.9624 | 0.5853 | 0.9454 | 0.9446 | 0.6364 | 0.9781 | 0.9634 | 0.3913 | 0.9128 | 0.9065 | 0.8635 |
| Increase | +0.0187 | +0.0126 | -0.1553 | +0.0186 | +0.0152 | -0.1328 | +0.0548 | +0.0512 | -0.2517 | +0.0137 | +0.0168 | -0.1063 | +0.0585 | +0.0627 | -0.2354 |
| DISTS | 0.9240 | 0.9153 | 0.8784 | 0.9539 | 0.9515 | 0.6629 | 0.9643 | 0.9562 | 0.5172 | 0.9659 | 0.9442 | 0.4871 | 0.8374 | 0.8296 | 1.1556 |
| O-DISTS | 0.9549 | 0.9424 | 0.6821 | 0.9709 | 0.9685 | 0.5294 | 0.9734 | 0.9694 | 0.4470 | 0.9701 | 0.9524 | 0.4568 | 0.8833 | 0.8752 | 0.9914 |
| Increase | +0.0309 | +0.0271 | -0.1963 | +0.0169 | +0.0170 | -0.1335 | +0.0092 | +0.0132 | -0.0701 | +0.0042 | +0.0082 | -0.0302 | +0.0458 | +0.0456 | -0.1642 |
| Avg. increase | +0.0213 | +0.0269 | -0.1329 | +0.0153 | +0.0131 | -0.1038 | +0.0551 | +0.0558 | -0.2045 | +0.0000 | -0.0002 | -0.0090 | +0.0441 | +0.0465 | -0.1521 |

Table 3. Performance comparison of omnidirectional IQA methods on the omnidirectional IQA database [14]. The best results are highlighted in bold.

empirical expectation over several preferable types of viewing behavior. Specifically, we sampled four different starting points evenly spaced along the equator. Example viewports extracted from the four starting points of a panorama are shown in Fig. 4. According to the subjective tests in [14, 15, 21–23], most viewers finish exploring panoramas of diverse content variations within 20 seconds. Thus, we set a fixed exploration time T to 15 seconds. To keep the computational complexity manageable, we designed a single scanpath by taking into account the fact that the front and equator regions are viewed more frequently than other parts (see Fig. 5). The user first browses the panorama from the starting point $(\phi_0, 0)$, then gradually moves the gaze counterclockwise along the equator to $(\phi_0 - \pi/2, 0)$ for viewing the left part of the 360° image. Next, the user begins to explore the right part of the scene by moving the gaze clockwise from $(\phi_0 - \pi/2, 0)$ to $(\phi_0 + \pi/2, 0)$. Finally, the user returns to the starting point $(\phi_0, 0)$ and finishes the browsing. Note that we constrained the gaze movements along the equator by clamping the latitude to $\theta = 0$. This results in four types of viewing behavior, whose detailed specifications are summarized in Table 2. In addition, the sampling rate is defined by

$$R = \frac{1}{s_2} \times v, \quad (10)$$

where s_2 is a stride parameter. v is the average gaze speed:

$$v = \frac{|P(t)|}{T}, \quad (11)$$

where $|P(t)|$ is the length of the scanpath.

4 EXPERIMENTS

In this section, we first described the implementation details of the proposed framework for omnidirectional IQA. Then, we introduced the evaluation procedures and compared our methods with state-of-the-art quality measures for this application. Last, we conducted comprehensive ablation studies to analyze the influence and sensitivity of individual components.

4.1 Implementation Details

Given a pair of reference and distorted panoramas, we first downsampled them to reduce the computational complexity as suggested in [20]. We then converted static panoramas into moving camera videos using

the default viewing behavior. The stride parameter s_2 in Eq. (10) was set to $\pi/75$, giving rise to $N = 150$ video frames for each panorama. In the stage of quality computation, the implementations of the five full-reference IQA models were obtained from the respective authors. The three parameters in the temporal hysteresis model, including the memory duration $K = 20$, the normalized Gaussian weighting function w with standard deviation $(2K - 1)/12$, and the linear factor $\alpha = 0.8$, were set according to [42].

4.2 Evaluation Protocols

We used two subject-rated VR datasets - the omnidirectional IQA database [14] and the LIVE 3D VR IQA database [15] to conduct the comparison experiments. The former contains 320 distorted panoramas in equirectangular projection format with resolution ranging from $11,332 \times 5,666$ to $11,320 \times 6,660$. These are generated from 16 reference panoramas with four distortion types at five distortion levels, including JPEG compression (JPEG), JPEG2000 compression (JP2K), Gaussian noise (GN), and Gaussian blur (GB). The latter includes 15 reference stereoscopic omnidirectional panoramas in equirectangular projection format with resolution of $4,096 \times 2,048$. Six distortion types with five levels are applied to produce 450 distorted images, including GN, GB, downsampling (DS), stitching distortion (ST), VP9 compression (VP9), and H.265 compression (H.265).

We used three evaluation metrics to quantify the quality prediction performance, including Pearson linear correlation coefficient (PLCC), Spearman rank-order correlation coefficient (SRCC), and root-mean-square error (RMSE). A better quality model achieves higher PLCC and SRCC values, and lower RMSE values. Before calculating PLCC and RMSE, we map model predictions to subjective quality ratings through a five-parameter logistic function:

$$f(Q) = \beta_1 \left(\frac{1}{2} - \frac{1}{1 + e^{\beta_2(Q - \beta_3)}} \right) + \beta_4 + \beta_5, \quad (12)$$

where $\{\beta_i\}_{i=1}^5$ are the parameters to be fitted.

4.3 Main Results

As stated in Sect. 3.4, we employed five state-of-the-art full-reference IQA methods - PSNR, SSIM [20], VIF [16], NLPD [17], and DISTS [18] to evaluate the frame-level quality of video representations of 360° images. We added an ‘‘O-’’ to these IQA methods as a prefix to

| | GB | GN | ST | VP9 | H.265 | DS | Overall |
|---------------|---------------|---------------|---------------|---------------|---------------|---------------|---------------|
| S-PSNR | 0.8883 | 0.8968 | 0.6580 | 0.6093 | 0.8066 | 0.8735 | 0.7292 |
| S-SSIM | 0.9021 | 0.9204 | 0.6342 | 0.7844 | 0.8745 | 0.8824 | 0.7500 |
| WS-PSNR | 0.8884 | 0.8968 | 0.6557 | 0.6086 | 0.8061 | 0.8738 | 0.7292 |
| CPP-PSNR | 0.8858 | 0.8977 | 0.6384 | 0.6107 | 0.8001 | 0.8734 | 0.7275 |
| PSNR | 0.8780 | 0.8962 | 0.6258 | 0.5722 | 0.7803 | 0.8632 | 0.7153 |
| O-PSNR | 0.9176 | 0.8929 | 0.7044 | 0.7483 | 0.8853 | 0.8877 | 0.7630 |
| Increase | + 0.0396 | - 0.0033 | + 0.0786 | + 0.1762 | + 0.1050 | + 0.0245 | + 0.0477 |
| SSIM | 0.8911 | 0.9129 | 0.5659 | 0.7695 | 0.8475 | 0.8761 | 0.7354 |
| O-SSIM | 0.9224 | 0.9244 | 0.6738 | 0.8226 | 0.9284 | 0.9099 | 0.7694 |
| Increase | + 0.0313 | + 0.0115 | + 0.1079 | + 0.0531 | + 0.0808 | + 0.0338 | + 0.0340 |
| VIF | 0.9430 | 0.9352 | 0.6919 | 0.8388 | 0.9142 | 0.9236 | 0.8420 |
| O-VIF | 0.9517 | 0.9267 | 0.7839 | 0.8769 | 0.9415 | 0.9242 | 0.7920 |
| Increase | + 0.0087 | - 0.0085 | + 0.0919 | + 0.0381 | + 0.0273 | + 0.0006 | - 0.0500 |
| NLPD | 0.9234 | 0.9235 | 0.6591 | 0.8790 | 0.9302 | 0.8844 | 0.6589 |
| O-NLPD | 0.9402 | 0.9310 | 0.7281 | 0.8663 | 0.9465 | 0.8983 | 0.7412 |
| Increase | + 0.0167 | + 0.0076 | + 0.0690 | - 0.0127 | + 0.0163 | + 0.0139 | + 0.0823 |
| DISTS | 0.9568 | 0.9212 | 0.6644 | 0.7380 | 0.8544 | 0.9388 | 0.7490 |
| O-DISTS | 0.9591 | 0.9004 | 0.7086 | 0.8016 | 0.8954 | 0.9536 | 0.8501 |
| Increase | + 0.0023 | - 0.0207 | + 0.0441 | + 0.0636 | + 0.0410 | + 0.0148 | + 0.1011 |
| Avg. increase | + 0.0197 | - 0.0027 | + 0.0783 | + 0.0637 | + 0.0541 | + 0.0175 | + 0.0430 |

Table 4. PLCC results of omnidirectional IQA methods on the LIVE 3D VR IQA database.

| | GB | GN | ST | VP9 | H.265 | DS | Overall |
|---------------|---------------|---------------|---------------|---------------|---------------|---------------|---------------|
| S-PSNR | 0.7584 | 0.8627 | 0.6382 | 0.5945 | 0.7970 | 0.7799 | 0.6490 |
| S-SSIM | 0.8101 | 0.9053 | 0.6124 | 0.7559 | 0.8736 | 0.7780 | 0.7217 |
| WS-PSNR | 0.7583 | 0.8633 | 0.6344 | 0.5947 | 0.7966 | 0.7793 | 0.6491 |
| CPP-PSNR | 0.7502 | 0.8793 | 0.6150 | 0.5819 | 0.7875 | 0.7762 | 0.6456 |
| PSNR | 0.7301 | 0.8569 | 0.6120 | 0.5610 | 0.7659 | 0.7856 | 0.6420 |
| O-PSNR | 0.8407 | 0.8476 | 0.6929 | 0.7222 | 0.8876 | 0.8124 | 0.6721 |
| Increase | + 0.1106 | - 0.0094 | + 0.0809 | + 0.1611 | + 0.1216 | + 0.0268 | + 0.0301 |
| SSIM | 0.7807 | 0.8976 | 0.5419 | 0.7426 | 0.8436 | 0.7593 | 0.7044 |
| O-SSIM | 0.8625 | 0.9112 | 0.6402 | 0.7847 | 0.9304 | 0.8254 | 0.7159 |
| Increase | + 0.0818 | + 0.0135 | + 0.0983 | + 0.0420 | + 0.0868 | + 0.0661 | + 0.0115 |
| VIF | 0.8928 | 0.9215 | 0.6942 | 0.8193 | 0.9182 | 0.8058 | 0.8333 |
| O-VIF | 0.9138 | 0.9052 | 0.7545 | 0.8735 | 0.9455 | 0.8137 | 0.7534 |
| Increase | + 0.0211 | - 0.0163 | + 0.0603 | + 0.0542 | + 0.0274 | + 0.0079 | - 0.0799 |
| NLPD | 0.8599 | 0.9128 | 0.6458 | 0.8613 | 0.9310 | 0.7896 | 0.6211 |
| O-NLPD | 0.8953 | 0.9200 | 0.7186 | 0.8448 | 0.9522 | 0.8128 | 0.7014 |
| Increase | + 0.0354 | + 0.0072 | + 0.0727 | - 0.0165 | + 0.0213 | + 0.0232 | + 0.0803 |
| DISTS | 0.9208 | 0.9103 | 0.6490 | 0.7084 | 0.8554 | 0.8516 | 0.7479 |
| O-DISTS | 0.9262 | 0.8877 | 0.7029 | 0.7810 | 0.8896 | 0.9380 | 0.8507 |
| Increase | + 0.0054 | - 0.0226 | + 0.0539 | + 0.0726 | + 0.0343 | + 0.0864 | + 0.1027 |
| Avg. increase | + 0.0509 | - 0.0055 | + 0.0732 | + 0.0627 | + 0.0583 | + 0.0421 | + 0.0289 |

Table 5. SRCC results of omnidirectional IQA methods on the LIVE 3D VR IQA database.

| | GB | GN | ST | VP9 | H.265 | DS | Overall |
|---------------|---------------|---------------|---------------|---------------|---------------|---------------|---------------|
| S-PSNR | 5.2906 | 4.0349 | 5.7850 | 6.7481 | 6.8063 | 6.4798 | 7.8074 |
| S-SSIM | 4.9706 | 3.5660 | 5.9401 | 5.2788 | 5.5846 | 6.2621 | 7.5472 |
| WS-PSNR | 5.2889 | 4.0349 | 5.8008 | 6.7532 | 6.8132 | 6.4716 | 7.8083 |
| CPP-PSNR | 5.3468 | 4.0185 | 5.9131 | 6.7391 | 6.9072 | 6.4805 | 7.8282 |
| PSNR | 5.5142 | 4.0461 | 5.9923 | 6.9798 | 7.2009 | 6.7179 | 7.9737 |
| O-PSNR | 4.5802 | 4.1068 | 5.4530 | 5.6465 | 5.3547 | 6.1260 | 7.3752 |
| Increase | - 0.9339 | + 0.0607 | - 0.5393 | - 1.3334 | - 1.8462 | - 0.5919 | - 0.5985 |
| SSIM | 5.2279 | 3.7233 | 6.3339 | 5.4348 | 6.1107 | 6.4211 | 7.7319 |
| O-SSIM | 4.4489 | 3.4790 | 5.6769 | 4.8392 | 4.2789 | 5.5212 | 7.2884 |
| Increase | - 0.7790 | - 0.2443 | - 0.6571 | - 0.5957 | - 1.8318 | - 0.8999 | - 0.4435 |
| VIF | 3.8337 | 3.2289 | 5.5464 | 4.6337 | 4.6657 | 5.1018 | 6.1559 |
| O-VIF | 3.5385 | 3.4278 | 4.7701 | 4.0906 | 3.8811 | 5.0819 | 6.9665 |
| Increase | - 0.2952 | + 0.1989 | - 0.7763 | - 0.5431 | - 0.7846 | - 0.0198 | + 0.8106 |
| NLPD | 4.4212 | 3.4993 | 5.7779 | 4.0578 | 4.2272 | 6.2101 | 8.5824 |
| O-NLPD | 3.9253 | 3.3287 | 5.2664 | 4.2507 | 3.7172 | 5.8471 | 7.6594 |
| Increase | - 0.4959 | - 0.1706 | - 0.5116 | + 0.1929 | - 0.5100 | - 0.3630 | - 0.9231 |
| DISTS | 3.3542 | 3.5496 | 5.7416 | 5.7432 | 5.9837 | 4.5859 | 7.5601 |
| O-DISTS | 3.2617 | 3.9671 | 5.4211 | 5.0886 | 5.1271 | 4.0060 | 6.0088 |
| Increase | - 0.0925 | + 0.4176 | - 0.3205 | - 0.6546 | - 0.8565 | - 0.5800 | - 1.5512 |
| Avg. increase | - 0.5193 | + 0.0525 | - 0.5609 | - 0.5868 | - 1.1658 | - 0.4909 | - 0.5411 |

Table 6. RMSE results of omnidirectional IQA methods on the LIVE 3D VR IQA database.

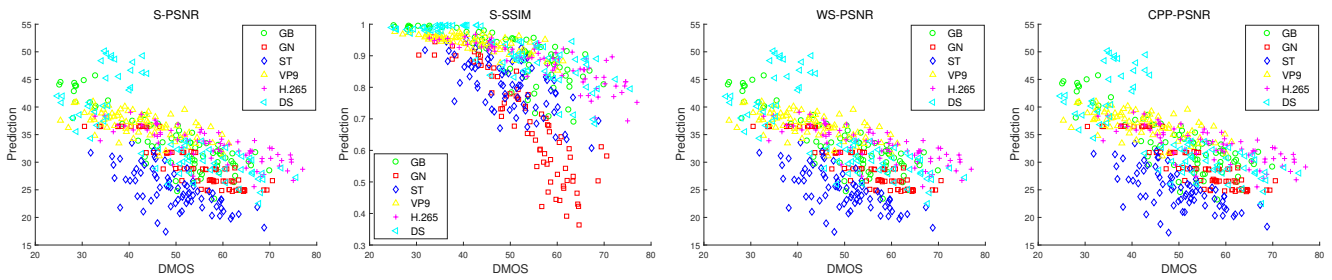


Fig. 6. Scatter plots of predictions from state-of-the-art omnidirectional IQA models against DMOSs from the LIVE 3D VR IQA database [15].

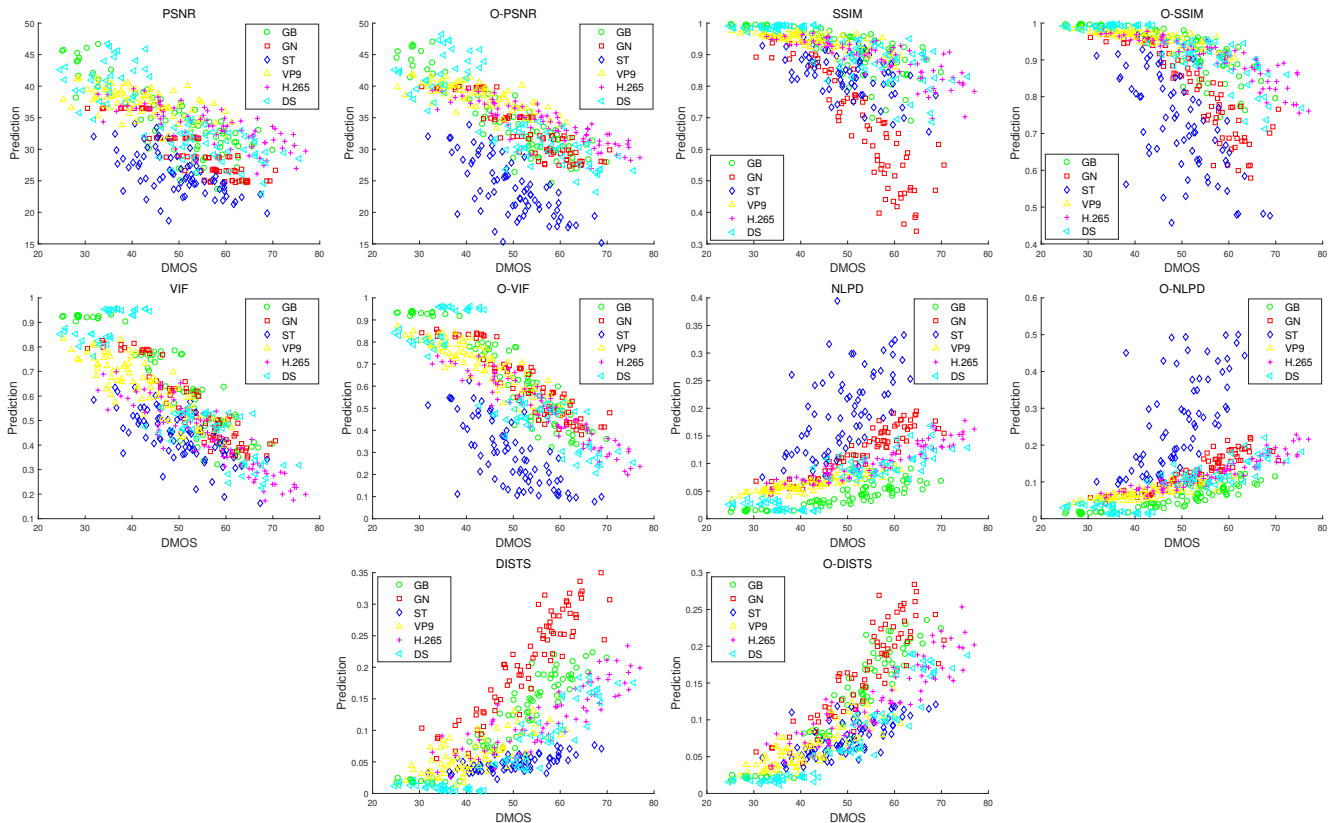


Fig. 7. Scatter plots of predictions from the five 2D IQA models and their corresponding omnidirectional versions against DMOSs from the LIVE 3D VR IQA database.

name our models (e.g., PSNR to O-PSNR). We included S-PSNR [7], S-SSIM [6], WS-PSNR [5], and CPP-PSNR [19] as representative omnidirectional IQA models for comparison. We also directly applied the five 2D IQA models to equirectangular projections to measure the relative perceptual gains by incorporating viewing behavior. For all models, we computed quality values on panoramas of the same downscaled resolution. The quality score of a stereoscopic image was computed by averaging quality scores of the left-view and right-view images. We listed the quantitative results on the omnidirectional IQA database and the LIVE 3D VR IQA database in Table 3, and Table 4, Table 5 and Table 6, respectively. We also drew scatter plots of model predictions versus the difference MOSs (DMOSs) on the LIVE 3D VR IQA database in Fig. 6 and Fig. 7.

From the experimental results, we made several interesting observations. First, it is quite surprising that recent 2D IQA models directly working with equirectangular projections outperform omnidirectional IQA models. For example, the performance of S-PSNR, S-SSIM, WS-PSNR, and CPP-PSNR are worse than that of VIF, NLPD, and DISTs on the omnidirectional IQA database. This suggests that instead of sticking to standard quality measures - PSNR and SSIM, we may

directly transfer recent advances in the domain of 2D IQA to VR applications. The fact that visual distortions in the VR databases have a large overlap with those in traditional IQA databases is indicative of the fact that recent 2D IQA models may work reasonably well. Second, we achieved significant performance improvements when applying existing IQA measures within the proposed quality assessment framework. Compared to assessing quality on equirectangular projections, the performance gains averaged over the five IQA models in terms of PLCC and SRCC can be as high as 0.0440 and 0.0465, respectively, on the omnidirectional IQA database. In particular, O-NLPD and O-DISTS rank the best on the omnidirectional IQA database and the LIVE 3D VR IQA database, respectively. Third, nearly all models tend to over-penalize stitching distortions, as most easily seen in Fig. 6 and Fig. 7. This explains the only exception in our experiments, where O-VIF underperforms VIF on the LIVE 3D VR IQA database, despite that O-VIF exhibits noticeable performance improvements on other individual distortion types. The stitching distortions are visually perceived as “ghosting” artifacts (also referred to as “double exposure”, see Fig. 8). When comparing to other types of distortions (e.g., JPEG compression and Gaussian blur), stitching artifacts may be more acceptable to

| | | Omnidirectional IQA database | | | | | | LIVE 3D VR IQA database | | | | | |
|--------|------|------------------------------|-------------------|----------|-----------|---------------|------------|-------------------------|-------------------|----------|-----------|---------------|------------|
| | | Arithmetic | Hysteresis | Harmonic | Geometric | Minkowski | Percentile | Arithmetic | Hysteresis | Harmonic | Geometric | Minkowski | Percentile |
| O-PSNR | PLCC | 0.7724 | 0.7677 | 0.7715 | 0.7717 | 0.7721 | 0.7581 | 0.7665 | 0.7630 | 0.7653 | 0.7658 | 0.7674 | 0.7545 |
| | SRCC | 0.7842 | 0.7799 | 0.7830 | 0.7837 | 0.7843 | 0.7692 | 0.6910 | 0.6721 | 0.6827 | 0.6864 | 0.6957 | 0.6294 |
| | RMSE | 1.3428 | 1.3549 | 1.3451 | 1.3446 | 1.3436 | 1.3789 | 7.3277 | 7.3752 | 7.3441 | 7.3371 | 7.3162 | 7.4878 |
| O-SSIM | PLCC | 0.8729 | 0.8717 | 0.8727 | 0.8728 | 0.8729 | 0.8650 | 0.7765 | 0.7694 | 0.7742 | 0.7752 | 0.7779 | 0.7639 |
| | SRCC | 0.8625 | 0.8616 | 0.8624 | 0.8624 | 0.8626 | 0.8552 | 0.7375 | 0.7159 | 0.7283 | 0.7328 | 0.7413 | 0.6735 |
| | RMSE | 1.0317 | 1.0361 | 1.0324 | 1.0320 | 1.0314 | 1.0611 | 7.1897 | 7.2884 | 7.2221 | 7.2075 | 7.1692 | 7.3638 |

Table 7. Performance comparison of O-PSNR and O-SSIM with different temporal pooling strategies. The default pooling model is highlighted in bold.



Fig. 8. Example of the panorama with stitching artifacts. (a) and (b) are the same viewports extracted from the original and distorted panoramas, respectively.

| | Image size | Viewport size | PLCC | SRCC | RMSE |
|--------|---------------|------------------|---------------|---------------|---------------|
| O-PSNR | 4,440 × 2,220 | 740 × 740 | 0.6723 | 0.6768 | 1.5652 |
| | 1,903 × 952 | 317 × 317 | 0.7677 | 0.7799 | 1.3549 |
| | 1,024 × 512 | 171 × 171 | 0.7801 | 0.7920 | 1.3229 |
| O-SSIM | 4,440 × 2,220 | 740 × 740 | 0.7211 | 0.7155 | 1.4648 |
| | 1,903 × 952 | 317 × 317 | 0.8717 | 0.8616 | 1.0361 |
| | 1,024 × 512 | 171 × 171 | 0.8962 | 0.8873 | 0.9378 |

Table 8. Performance comparison of O-PSNR and O-SSIM with different input resolutions on the omnidirectional IQA database. The default setting is highlighted in bold.

the HVS, but cause significant structural fidelity loss, as reflected by predictions of several quality models. Finally, it is worth noting that the current results were based on the default viewing behavior. We expect that further performance gains may be obtained if the information regarding the true viewing behavior of users is available.

4.4 Ablation Experiments

In this subsection, we conducted a series of ablation experiments to analyze the impact of temporal pooling strategies, input resolutions, and sampling rates on the quality prediction performance.

Choice of Temporal Pooling Strategies In addition to the temporal hysteresis pooling [42], we tested another five strategies, including arithmetic mean, harmonic mean, geometric mean, Minkowski mean

| | s_2 | R | PLCC | SRCC | RMSE |
|--------|-----------|-----|---------------|---------------|---------------|
| O-PSNR | $\pi/45$ | 6 | 0.7631 | 0.7859 | 1.3522 |
| | $\pi/60$ | 8 | 0.7546 | 0.7827 | 1.3723 |
| | $\pi/75$ | 10 | 0.7677 | 0.7799 | 1.3549 |
| | $\pi/90$ | 12 | 0.7631 | 0.7859 | 1.3521 |
| | $\pi/105$ | 14 | 0.7631 | 0.7860 | 1.3522 |
| O-SSIM | $\pi/45$ | 6 | 0.8822 | 0.8515 | 1.0353 |
| | $\pi/60$ | 8 | 0.8677 | 0.8399 | 1.0837 |
| | $\pi/75$ | 10 | 0.8717 | 0.8616 | 1.0361 |
| | $\pi/90$ | 12 | 0.8822 | 0.8515 | 1.0353 |
| | $\pi/105$ | 14 | 0.8822 | 0.8515 | 1.0352 |

Table 9. Performance comparison of O-PSNR and O-SSIM with different sampling rates on the omnidirectional IQA database.

(using ℓ_2 -norm) and percentile scoring (using 10%) [43]. From Table 7, we found that no temporal pooling strategy seems to be significantly better than the others, when PSNR and SSIM were adopted as the base quality measures. The reasons may be twofold. First, most test panoramas are distorted globally, resulting in relatively uniform (and less time-varying) quality. Second, the temporal pooling effect may be further washed out by taking the expectation under the default viewing behavior. This suggests that the current VR IQA databases may not fully demonstrate the potentials of our methods. Since temporal pooling has been empirically verified to be more effective than simply average pooling in VQA [12,44], we believe the proposed framework would work equally well for 360° images suffering from non-uniform local distortions (*e.g.*, realistic camera distortions).

Choice of Input Resolutions The resolutions of the input 360° images determine the effective viewing distances and the sizes of viewports. We tested the proposed O-PSNR and O-SSIM with different input sizes, and showed the results on the omnidirectional IQA database in Table 8. It can be observed that the performance becomes better as the input resolution reduces. In our implementation, we employed automatic downsampling as suggested in [20] to keep the shorter side of the panorama in the range of [512, 1024]. Accordingly, the size of the square viewports is in the range of [171, 342]. As such, we balanced the signal fidelity due to downsampling and the computational complexity.

Choice of Sampling Rates In our proposed framework, we generated the video sequence by sampling viewports along the scanpath with a certain rate. Thus, it is natural to ask: what is the optimal sampling rate in terms of prediction accuracy and computational complexity? We tested our models with different sampling rates by adjusting the stride parameter s_2 , and listed the results on the omnidirectional IQA database in Table 9. We found that O-PSNR and O-SSIM are robust to variations of sampling rates due in part to the temporal uniformity of the distortions. When omnidirectional images are distorted non-uniformly, we expect that higher sampling rates would lead to more accurate predictions. In such cases, the computational cost would also increase.

5 CONCLUSION

We have introduced a principled framework to design objective omnidirectional IQA models, which incorporates user viewing behavior into the quality prediction process. The key idea is to map omnidirectional panoramas to moving camera videos by extracting the sequences of viewports along the scanpaths. Experimental results on two VR IQA databases demonstrated the promise of the proposed framework, where we successfully transferred the advances in 2D IQA to VR conditions.

We have tested our methods using panoramas with global uniform distortions only. How local non-uniform distortions influence the viewing behavior of users and in turn the perceived quality of panoramas is an interesting and challenging problem yet to be explored. We are currently building the first subjective VR database for this purpose, and further testing the generalizability of the proposed models.

Our framework suggests a natural extension to *personalized* omnidirectional IQA, which may be more suitable in VR applications as users' viewing behavior tends to vary based on their own personal experiences and preferences. This can be easily achieved by exploiting the viewing behavior statistics of a single user, instead of averaging across several viewers.

REFERENCES

- [1] "VR photography," 2020 (accessed Apr. 10, 2020). [Online]. Available: https://en.wikipedia.org/wiki/VR_photography
- [2] M. Xu, C. Li, S. Zhang, and P. L. Callet, "State-of-the-art in 360 video/image processing: Perception, assessment and compression," *IEEE Journal of Selected Topics in Signal Processing*, vol. 14, no. 1, pp. 5–26, Jan. 2020.
- [3] Z. Wang and A. C. Bovik, *Modern Image Quality Assessment*. San Rafael, CA, USA: Morgan Claypool Publishers, 2006.
- [4] King-To Ng, Shing-Chow Chan, and Heung-Yeung Shum, "Data compression and transmission aspects of panoramic videos," *IEEE Transactions on Circuits and Systems for Video Technology*, vol. 15, no. 1, pp. 82–95, Jan. 2005.
- [5] Y. Sun, A. Lu, and L. Yu, "Weighted-to-spherically-uniform quality evaluation for omnidirectional video," *IEEE Signal Processing Letters*, vol. 24, no. 9, pp. 1408–1412, Sep. 2017.
- [6] F. Lopes, J. Ascenso, A. Rodrigues, and M. P. Queluz, "Subjective and objective quality assessment of omnidirectional video," in *Applications of Digital Image Processing XLI*, vol. 10752, International Society for Optics and Photonics. SPIE, Sep. 2018, pp. 249–265.
- [7] M. Yu, H. Lakshman, and B. Girod, "A framework to evaluate omnidirectional video coding schemes," in *IEEE International Symposium on Mixed and Augmented Reality*, 2015, pp. 31–36.
- [8] S. Chen, Y. Zhang, Y. Li, Z. Chen, and Z. Wang, "Spherical structural similarity index for objective omnidirectional video quality assessment," in *IEEE International Conference on Multimedia and Expo*, 2018, pp. 1–6.
- [9] V. Sitzmann, A. Serrano, A. Pavel, M. Agrawala, D. Gutierrez, B. Masia, and G. Wetzstein, "Saliency in VR: How do people explore virtual environments?" *IEEE Transactions on Visualization and Computer Graphics*, vol. 24, no. 4, pp. 1633–1642, Apr. 2018.
- [10] D. Noton and L. Stark, "Scanpaths in saccadic eye movements while viewing and recognizing patterns," *Vision Research*, vol. 11, no. 9, pp. 929–938, Sep. 1971.
- [11] F. Dufaux and J. Konrad, "Efficient, robust, and fast global motion estimation for video coding," *IEEE Transactions on Image Processing*, vol. 9, no. 3, pp. 497–501, Mar. 2000.
- [12] Z. Tu, C.-J. Chen, L.-H. Chen, N. Birkbeck, B. Adsumilli, and A. C. Bovik, "A comparative evaluation of temporal pooling methods for blind video quality assessment," *CoRR*, vol. abs/2002.10651, 2020. [Online]. Available: <https://arxiv.org/abs/2002.10651>
- [13] B. B. Murdock Jr, "The serial position effect of free recall," *Journal of Experimental Psychology*, vol. 64, no. 5, p. 482488, 1962.
- [14] H. Duan, G. Zhai, X. Min, Y. Zhu, Y. Fang, and X. Yang, "Perceptual quality assessment of omnidirectional images," in *IEEE International Symposium on Circuits and Systems*, 2018, pp. 1–5.
- [15] M. Chen, Y. Jin, T. Goodall, X. Yu, and A. C. Bovik, "Study of 3D virtual reality picture quality," *IEEE Journal of Selected Topics in Signal Processing*, vol. 14, no. 1, pp. 89–102, Jan. 2020.
- [16] H. R. Sheikh, A. C. Bovik, and G. de Veciana, "An information fidelity criterion for image quality assessment using natural scene statistics," *IEEE Transactions on Image Processing*, vol. 14, no. 12, pp. 2117–2128, Dec. 2005.
- [17] V. Laparra, A. Berardino, J. Ballé, and E. P. Simoncelli, "Perceptually optimized image rendering," *Journal of the Optical Society of America A*, vol. 34, no. 9, p. 1511, Sep. 2017.
- [18] K. Ding, K. Ma, S. Wang, and E. P. Simoncelli, "Image quality assessment: Unifying structure and texture similarity," *CoRR*, vol. abs/2004.07728, 2020. [Online]. Available: <https://arxiv.org/abs/2004.07728>
- [19] V. Zakharchenko, K. P. Choi, and J. H. Park, "Quality metric for spherical panoramic video," in *Optics and Photonics for Information Processing X*, vol. 9970, International Society for Optics and Photonics. SPIE, Sep. 2016, pp. 57–65.
- [20] Z. Wang, A. C. Bovik, H. R. Sheikh, and E. P. Simoncelli, "Image quality assessment: From error visibility to structural similarity," *IEEE Transactions on Image Processing*, vol. 13, no. 4, pp. 600–612, Apr. 2004.
- [21] E. Upenik, M. ebek, and T. Ebrahimi, "Testbed for subjective evaluation of omnidirectional visual content," in *Picture Coding Symposium*, 2016, pp. 1–5.
- [22] W. Sun, K. Gu, S. Ma, W. Zhu, N. Liu, and G. Zhai, "A large-scale compressed 360-degree spherical image database: From subjective quality evaluation to objective model comparison," in *IEEE 20th International Workshop on Multimedia Signal Processing*, 2018, pp. 1–6.
- [23] M. Huang, Q. Shen, Z. Ma, A. C. Bovik, P. Gupta, R. Zhou, and X. Cao, "Modeling the perceptual quality of immersive images rendered on head mounted displays: Resolution and compression," *IEEE Transactions on Image Processing*, vol. 27, no. 12, pp. 6039–6050, Dec. 2018.
- [24] J. Johnson, A. Alahi, and L. Fei-Fei, "Perceptual losses for real-time style transfer and super-resolution," in *European Conference on Computer Vision*, 2016, pp. 694–711.
- [25] R. Zhang, P. Isola, A. A. Efros, E. Shechtman, and O. Wang, "The unreasonable effectiveness of deep features as a perceptual metric," in *IEEE Conference on Computer Vision and Pattern Recognition*, 2018, pp. 586–595.
- [26] K. Zeng and Z. Wang, "3D-SSIM for video quality assessment," in *IEEE International Conference on Image Processing*, 2012, pp. 621–624.
- [27] W. Kim, J. Kim, S. Ahn, J. Kim, and S. Lee, "Deep video quality assessor: From spatio-temporal visual sensitivity to a convolutional neural aggregation network," in *European Conference on Computer Vision*, 2018, pp. 219–234.
- [28] M. Xu, J. Chen, H. Wang, S. Liu, G. Li, and Z. Bai, "C3DVQA: Full-reference video quality assessment with 3d convolutional neural network," *CoRR*, vol. abs/1910.13646, 2019. [Online]. Available: <http://arxiv.org/abs/1910.13646>
- [29] G. Luz, J. Ascenso, C. Brites, and F. Pereira, "Saliency-driven omnidirectional imaging adaptive coding: Modeling and assessment," in *IEEE 19th International Workshop on Multimedia Signal Processing (MMSp)*, Oct. 2017, pp. 1–6.
- [30] M. Xu, C. Li, Z. Chen, Z. Wang, and Z. Guan, "Assessing visual quality of omnidirectional videos," *IEEE Transactions on Circuits and Systems for Video Technology*, vol. 29, no. 12, pp. 3516–3530, Dec. 2019.
- [31] D. S. Hands and S. E. Avons, "Recency and duration neglect in subjective assessment of television picture quality," *Applied Cognitive Psychology*, vol. 15, no. 6, pp. 639–657, Nov. 2001.
- [32] Y. Ye, E. Alshina, and J. Boyce, "JVET-G1003: Algorithm description of projection format conversion and video quality metrics in 360lib version 4," Joint Video Exploration Team, Turin, Italy, Rep. JVET-G1003, Tech. Rep., Jul. 2017.
- [33] J. Besharse and D. Bok, *The Retina And Its Disorders*. Academic Press, 2011.
- [34] Z. Wang, E. P. Simoncelli, and A. C. Bovik, "Multiscale structural similarity for image quality assessment," in *The Thirty-Seventh Asilomar Conference on Signals, Systems Computers*, vol. 2, 2003, pp. 1398–1402.
- [35] S. S. Channappayya, A. C. Bovik, C. Caramanis, and R. W. Heath, "SSIM-optimal linear image restoration," in *IEEE International Conference on Acoustics, Speech and Signal Processing*, 2008, pp. 765–768.
- [36] J. Ballé, D. Minnen, S. Singh, S. J. Hwang, and N. Johnston, "Variational image compression with a scale hyperprior," *CoRR*, vol. abs/1802.01436, 2018. [Online]. Available: <http://arxiv.org/abs/1802.01436>
- [37] J. Snell, K. Ridgeway, R. Liao, B. D. Roads, M. C. Mozer, and R. S. Zemel, "Learning to generate images with perceptual similarity metrics," in *IEEE International Conference on Image Processing*, 2017, pp. 4277–4281.
- [38] S. Wang, A. Rehman, Z. Wang, S. Ma, and W. Gao, "SSIM-motivated rate-distortion optimization for video coding," *IEEE Transactions on Circuits and Systems for Video Technology*, vol. 22, no. 4, pp. 516–529, Apr. 2012.
- [39] H. R. Sheikh, A. C. Bovik, and G. de Veciana, "An information fidelity criterion for image quality assessment using natural scene statistics," *IEEE Transactions on Image Processing*, vol. 14, no. 12, pp. 2117–2128, Dec. 2005.
- [40] Netflix, "Toward a practical perceptual video quality metric," 2016. [Online]. Available: <https://medium.com/netflix-techblog/toward-a-practical-perceptual-video-quality-metric-653f208b9652>
- [41] K. Ding, K. Ma, S. Wang, and E. P. Simoncelli, "Comparison of image quality models for optimization of image processing systems," *CoRR*, vol. abs/2005.01338, 2020. [Online]. Available: <https://arxiv.org/abs/2005.01338>
- [42] K. Seshadrinathan and A. C. Bovik, "Temporal hysteresis model of time varying subjective video quality," in *IEEE International Conference on Acoustics, Speech and Signal Processing*, 2011, pp. 1153–1156.
- [43] A. K. Moorthy and A. C. Bovik, "Visual importance pooling for image quality assessment," *IEEE Journal of Selected Topics in Signal Processing*, vol. 3, no. 2, pp. 193–201, Apr. 2009.
- [44] S. Rimac-Drlje, M. Vranjes, and D. Zagar, "Influence of temporal pooling method on the objective video quality evaluation," in *IEEE International Symposium on Broadband Multimedia Systems and Broadcasting*, 2009, pp. 1–19.